ELSEVIER

#### Contents lists available at ScienceDirect

#### **Biomaterials**

journal homepage: www.elsevier.com/locate/biomaterials





## Matching mechanical heterogeneity of the native spinal cord augments axon infiltration in 3D-printed scaffolds

Kiet A. Tran <sup>a</sup>, Brandon J. DeOre <sup>a</sup>, David Ikejiani <sup>b</sup>, Kristen Means <sup>b</sup>, Louis S. Paone <sup>a</sup>, Laura De Marchi <sup>a</sup>, Łukasz Suprewicz <sup>c</sup>, Katarina Koziol <sup>a</sup>, Julien Bouyer <sup>d</sup>, Fitzroy J. Byfield <sup>e</sup>, Ying Jin <sup>d</sup>, Penelope Georges <sup>f</sup>, Itzhak Fischer <sup>d</sup>, Paul A. Janmey <sup>e</sup>, Peter A. Galie <sup>a</sup>, <sup>\*</sup>

- <sup>a</sup> Department of Biomedical Engineering, Rowan University, Glassboro, NJ, USA
- <sup>b</sup> Department of Bioengineering, Rice University, Houston, TX, USA
- <sup>c</sup> Department of Medical Microbiology and Nanobiomedical Engineering, Medical University of Bialystok, Bialystok, Poland
- <sup>d</sup> Department of Neurobiology and Anatomy, Drexel College of Medicine, Philadelphia, PA, USA
- <sup>e</sup> Department of Physiology, University of Pennsylvania, Philadelphia, PA, USA
- f Council on Science and Technology, Princeton University, Princeton, NJ, USA

#### ARTICLE INFO

# Keywords: 3D-printing Digital light processing Rheology Spinal cord injury Axon regeneration Tissue engineering

#### ABSTRACT

Scaffolds delivered to injured spinal cords to stimulate axon connectivity often match the anisotropy of native tissue using guidance cues along the rostral-caudal axis, but current approaches do not mimic the heterogeneity of host tissue mechanics. Although white and gray matter have different mechanical properties, it remains unclear whether tissue mechanics also vary along the length of the cord. Mechanical testing performed in this study indicates that bulk spinal cord mechanics do differ along anatomical level and that these differences are caused by variations in the ratio of white and gray matter. These results suggest that scaffolds recreating the heterogeneity of spinal cord tissue mechanics must account for the disparity between gray and white matter. Digital light processing (DLP) provides a means to mimic spinal cord topology, but has previously been limited to printing homogeneous mechanical properties. We describe a means to modify DLP to print scaffolds that mimic spinal cord mechanical heterogeneity caused by variation in the ratio of white and gray matter, which improves axon infiltration compared to controls exhibiting homogeneous mechanical properties. These results demonstrate that scaffolds matching the mechanical heterogeneity of white and gray matter improve the effectiveness of biomaterials transplanted within the injured spinal cord.

#### 1. Introduction

A potential benefit of transplanting bioengineered scaffolds is the delivery of a matrix with mechanical properties that mimic the host tissue, but the mechanics of native tissue are often heterogeneous and difficult to characterize. In particular, our understanding of the mechanical properties of the central nervous system (CNS), specifically the spinal cord, is primarily informed by macroscale measurements [1–3]. These studies show that CNS mechanics are heterogenous via tensile, shear, compression testing [4,5] and magnetic resonance elastography [6,7]. In order to supplement bulk approaches, atomic force microscopy (AFM) is a useful tool to measure the stiffness of the spinal cord with higher spatial resolution. However, published data are contradictory regarding the difference in mechanical properties between white and

gray matter [8–10]. Physiologically, white and gray matter exhibit differences in cellular and matrix composition: white matter mainly consists of glial cells and myelinated axons aligned along the rostral-caudal direction, whereas gray matter is mostly comprised of neuronal cell bodies, which likely alters its mechanical properties. Moreover, the complex and variable environment of a spinal cord injury (SCI) alters cord mechanics [11]. Therefore, transplanting a scaffold that mimics the mechanical heterogeneity of white and gray matter may improve axon infiltration at the site of spinal cord injury.

Several studies have interrogated the effect of injury on the mechanical properties of the spinal cord. In the aftermath of a spinal cord injury, an influx of inflammatory cytokines and localized ischemia impose a biochemical barrier, while the formation of a glial scar alters the composition and the mechanical properties of the cord tissue that

E-mail address: galie@rowan.edu (P.A. Galie).

<sup>\*</sup> Corresponding author.

mitigates axon growth [12,13]. Studies using AFM to characterize cord mechanics after injury indicate that the tissue undergoes an initial decrease in stiffness in a complex process that involves alteration to the cord extracellular matrix, cell death, and axon retraction and demyelination. Therefore, axons attempting to bridge the site of CNS injuries face an insurmountable challenge, in part due to the body's own response to the damage. One potential treatment strategy currently being investigated in clinical trials is the use of implantable scaffolds to aid axon growth at the site of injury.

Bioengineered scaffolds with a wide array of mechanical properties have previously been used in spinal cord injury. The overall goal of transplanted hydrogels or conduits is to bridge the injured area by facilitating axon connectivity and eventual functional recovery for patients. Previously used scaffolds in animal studies and human clinical trials incorporate a wide variety of biomaterials including collagen [14], polycaprolactone [15-18], electrospun fibers [19-21], fibrin [22-24] and can either be injected [25,26] or delivered as solid conduits [14]. These approaches use several repair strategies including delivery of neurotrophic factors or cells [27], implementation of a conductive microenvironment using electrically active materials [28], and providing guidance cues by anisotropic topologies including cylindrical voids [16,29,30]. Considerations for biomaterials used in previous spinal cord scaffolds include biocompatibility, degradability, permissivity to infiltrating axons from the host, and matching approximate, bulk mechanical properties of the spinal cord [31]. Yet, none of the previous approaches tune the mechanical heterogeneity within the construct as a potential repair strategy for spinal cord regeneration.

3D-printed scaffolds provide a means to fabricate heterogeneous mechanical properties that match native spinal cord tissue. Previous approaches have demonstrated that photocrosslinkable hydrogels can be used in 3D-printed systems that can mimic the anisotropy of various tissues including skeletal muscle [32], bone [33-35], cartilage [36-39], and neural tissue [40,41]. 3D-printing has also been used to fabricate spinal cord conduits that feature voids aligned in the rostral-caudal to mimic specific axon tracts [42]. However, the scaffolds in that particular study exhibited an elastic modulus exceeding 200 kPa, which far surpasses the mechanical properties of the surrounding spinal cord tissue and precludes the ability to differentiate between the stiffness of white and gray matter. Recent innovations in 3D-printing approach, specifically digital light processing (DLP) have been used to create complex topologies within tunable 3D scaffolds that overcomes the limitations of previous strategies [43,44]. This process can control and guide the growth of axons in scaffolds with heterogeneous mechanical properties to facilitate both infiltration and outgrowth from the site of injury. In this study, an array of macroscale and microscale mechanical tests are used to characterize the mechanical properties of native spinal cord tissue, which then inform a DLP-based approach to mimic the mechanical heterogeneity in transplantable scaffolds.

#### 2. Materials and methods

#### 2.1. Solution preparation

Dissecting and measuring artificial cerebrospinal fluids were formulated to maintain the viability of isolated spinal cords using previous methods [45,46]. Briefly, dissecting artificial cerebrospinal fluid (*d*-aCSF) was supplemented with 191 mM sucrose, 0.75 mM K-gluconate, 1.25 mM KH<sub>2</sub>PO<sub>4</sub>, 26 mM NaHCO<sub>3</sub>, 4 mM MgSO<sub>4</sub>, 1 mM CaCl<sub>2</sub>, 20 mM glucose, 2 mM kynurenic acid, 1 mM (+)-sodium L-ascorbate, 5 mM ethyl pyruvate, 3 mM myo-inositol, and 2 mM NaOH. Additionally, measuring artificial cerebrospinal fluid (*m*-aCSF) was composed of 121 mM NaCl, 3 mM KCl, 1.25 mM NaH<sub>2</sub>PO<sub>4</sub>, 25 mM NaHCO<sub>3</sub>, 1.1 mM MgCl<sub>2</sub>, 2.2 mM CaCl<sub>2</sub>, 15 mM glucose, 1 mM sodium L(+)-ascorbate, 5 mM ethyl pyruvate, and 3 mM myo-inositol. The resulting pH of these solutions was ~7.3. All the above reagents were purchased from VWR.

#### 2.2. Spinal cord preparation

Bovine spinal cords were severed at the C3 level and isolated directly into quart-sized containers of ice-cold dissecting artificial cerebrospinal fluid (d-aCSF) at Bringhurst Meats (Berlin, NJ). After measuring the lengths of the cords, each tissue was divided into three regions: cervical (between 31 and 35 inches from caudal end), lumbar (between 20 and 26 inches from caudal), and sacral (10 inches from caudal). All regions were cut along the transverse anatomical plane in approximately 5-6-mm slices, and then immersed in m-aCSF for testing. For mechanical testing of rat cords, an established technique for hydraulic extrusion was used on male Sprague Dawley rats provided by David Li of Dr. Rebecca Wells's laboratory at the University of Pennsylvania within an hour of sacrifice [47]. The cords were cut into approximately 5-6-mm transverse slices and adhered to a 60-mm Petri dish filled with m-aCSF.

#### 2.3. Spinal cord macroscale mechanical characterization

All spinal cord mechanics were examined within 1-2 h after extraction and experiments were performed within 6 h, as previous studies have shown that cords preserved in aCSF maintain their mechanical properties over this timespan [45]. The local mechanics of the gray and white matter were examined using AFM. Spinal cord sections were fixed to the petri dishes using transglutaminase that has been shown as a tissue adhesive [48] and fully embedded in m-aCSF during these measurements. AFM measurements were taken in triplicates in regions of both gray and white matter using a 20- $\mu$ m diameter silicon spherical tip with a cantilever spring constant of 0.6 N/m.

Rheology was conducted at several levels of compressive strain to characterize the macroscopic mechanical properties of the cord at different regions. Measurements were conducted on a rheometer (Kinexus) with a 20-mm parallel attachment. During rheological measurements, *m*-aCSF was pipetted around the tissue to prevent the cord from drying out. The gap was set with respect to the height of each spinal cord section. The bulk mechanical properties of the cords were evaluated by measuring the shear modulus at a steady frequency of 1 Hz and 1% strain for 90 s. The test was repeated for successive compression steps of 100 µm.

A Kibron tensiometer was used to measure the relaxation effects of the gray and white matter of bovine spinal cords. Tissue sections were submerged in *m*-aCSF during relaxation measurements. A 500-µm probe was lowered in the gray and white matter to interrogate the relaxation profiles within each matter region. The relaxation factors were calculated by measuring the decay in force with time after indentation.

#### 2.4. Synthesis of polymer and photoinitiator

The polymers and initiators for the prehydrogel solutions, including methacrylate (GelMA) and lithium trimethylbenzoylphosphinate (LAP), were synthesized as previously described [43]. In brief, GelMA was synthesized through dropwise addition of methacrylic anhydride to 10 wt% gelatin (Sigma, derived from porcine skin; type A; gel strength 300) in carbonate/bicarbonate buffer for 4 h at 50–55  $^{\circ}\text{C},$  then precipitated in ethanol. The precipitate was allowed to dry for multiple days before resuspension at 20 wt% in PBS. GelMA was sterilized with  $0.22 \mu m$  filters and stock solutions were aliquoted then stored at 20 °C until use. LAP was prepared by the reaction of dimethyl phenylphosphinite and 2,3,6-trimethylbenzoyl chloride under argon overnight at room temperature. Then 4 M excess lithium bromide dissolved in 2-butanone was added to the reaction mixture. The solution was heated to 50  $^{\circ}\text{C}$  for precipitation (~10–30 min), cooled to room temperature for 4 h then filtered with 2-butanone and diethyl ether. The resulting precipitate was allowed to dry for several days before storing under nitrogen at 4 °C until use. Stock solutions were prepared at 200 mM in PBS, sterile filtered, and protected from light until use.

#### 2.5. Preparation of 3D printed scaffolds

For all fabrication of hydrogel scaffolds, prehydrogel mixtures were prepared containing 15 wt% GelMA, 17 mM LAP, 2.255 mM tartrazine photoabsorber, and 10% glycerol in sterile 1x PBS. The Volumetric-α Bioprinter used in fabrication was previously developed by the Jordan Miller lab and Volumetric [43]. This stereolithography-based 3D printer used a polydimethylsiloxane (PDMS) coated Petri dish as a vat for the prehydrogel mixture and a build platform with a bonded frosted-glass slide onto which the cured gel would attach during printing. After transferring the prehydrogel solution into the vat, the build platform was then lowered to the first fabrication layer position to start printing. A custom Matlab script was used to create the 2D photomasks from a 3D model. Grayscale patterning was the method used for outputting a hydrogel with the desired mechanical heterogeneity of localized regions for the study. The grayscale patterning uses light intensity values between 0 and 100%, representing black to white, to change the extent of polymerization of the hydrogel. This process included an analysis of the 3-dimensional model, separating them into even 50-um sections in the z-direction, then applying the grayscaled pattern on top of the resulting slices to create the final photomasks. A built-in software on the printer was used to import the photomask and control the apparatus by sending GCode commands for vertical movement of the build platform and images to the projector. The photomasks are projected in sequence for a set exposure time of 14.5 s and light intensity of 20 mW/cm<sup>2</sup> (at 100% grayscale) for each projection to build the 3D hydrogel object through layer-by-layer photopolymerization. After printing was complete, the 3D fabricated hydrogels were removed from the glass slide of the build platform with a razor and equilibrated in multiple sterile PBS washes. The 3D models of T10 rat thoracic regions of the spinal cord were created in Blender. The grayscale light intensity value for the simulated white matter was 75% and the gray matter was 100%. These intensity values were chosen to create substantial heterogeneity in the scaffold stiffness without sacrificing the fidelity of the print. The hydrogels were printed in groupings of 8.

#### 2.6. Scanning electron microscopy (SEM)

The microstructure of 3D-printed GelMA hydrogels was examined using a scanning electron microscope (FEI SEM). The scaffolds were frozen with liquid nitrogen and lyophilized for 2 h. The freeze-dried samples were cut in cross-section and sputter coated for 30 s per sample. The porosity was analyzed by measuring pore diameters with the measure function in ImageJ.

#### 2.7. Atomic force microscopy (AFM) of 3D-printed scaffolds

For atomic force microscopy, raster scans (100  $\mu m \times 100~\mu m)$  were performed to generate force-distance curves on regions within the regions of gray matter, white matter, and regions that contain both the gray and white matter. The scaffolds were submerged in a-CSF during the AFM experiments. Measurements were employed using a 20- $\mu m$  silicon spherical tip with a spring constant of 0.6 N/m.

#### 2.8. Spinal cord surgery and transplantation

Animal surgeries were conducted at the Drexel University Queen Lane Medical Campus. All animal procedures were approved by the Institutional Animal Care and Use Committee of Drexel University College of Medicine (approval number: 20,938 21–26) and these experiments were performed according to the National Institutes of Health (NIH) Guide for the Care and Use of Laboratory Animals. Nine female Sprague-Dawley rats (225–250 g) were housed with a 12-h/12-h light/dark cycle in this study. These rats were administered with 5% of isoflurane until unconscious and the concentration of anesthesia was reduced to 3% during surgery. To create the transection spinal cord

injury model, a laminectomy was performed at the thoracic 10 (T10) level and aspiration was performed to remove the tenth level of the thoracic cord, leaving a cavity of approximate dimensions of 2 x 2  $\times$  2 mm. Upon transplantation, three scaffold conditions were employed: 1) homogeneous hydrogels exhibiting the stiffness of white matter, 2) homogenous hydrogels with the stiffness of gray matter, or 3) heterogeneous scaffolds that mimic the differences in gray and white matter based on the topology of the rat T10 cord. Muscles and skin were sutured and closed with clips. Buprenex (0.015–0.02 mg/kg) was subcutaneously administered after the surgery. The bladder was manually expressed twice a day until the end of the experiment. Animals were sacrificed 2 weeks after peptide injections.

#### 2.9. Bovine spinal cord immunohistochemistry

Bovine spinal cord sections were fixed with 4% paraformaldehyde on ice for 40 min. After fixation, the spinal sections were embedded in OCT compound and snap-frozen to cryopreserve the tissue and stored at 80 °C until processing. Each tissue region was sectioned at 20  $\mu m$  thickness in a cryostat and mounted onto gelatin-coated slides. The slides were washed with phosphate buffered saline (PBS) and sections were blocked with 1% bovine serum albumin (BSA) for 30 min at room temperature. Anti-myelin primary antibodies (VWR) were diluted at a ratio of 1:200 in dilution buffer consisting of 1% BSA (VWR), 0.3% Triton X-100 (Sigma), and 0.01 sodium azide (VWR) and incubated overnight at 2–8 °C. The slides were washed thoroughly with PBS and secondary antibodies were incubated at room temperature for 60 min at a ratio of 1:500. DAPI stains were added to each slide for an additional incubation time of 5 min at room temperature. Finally, sections were washed and mounted in anti-fade mounting media.

#### 2.10. Rat spinal cord immunohistology

Two weeks following transplantations, rats were overdosed with Euthasol (J. A. Webster) and transcardially perfused with 100 mL of 0.9% saline and 500 mL of 4% paraformaldehyde in phosphate buffer. Spinal cords were removed and incubated in 4% paraformaldehyde overnight and cryoprotected with 30% sucrose/0.1 M phosphate buffer at 4 °C for 3 days. The cords were transferred to M1 medium and cryosectioned with thicknesses of 20  $\mu m$ . Sagittal sections were separated into six sets (approximately 10–15 mm in length) with gelatin coated glass slides. Adjacent sections on glass slides were spaced approximately 120- $\mu m$  apart within the cord and the histological slides were kept at 20 °C.

Histological sections were thoroughly washed and blocked with 10% goat or donkey serum for 1 h prior to immunohistochemical staining. Sections were selected for immunohistochemical staining using primary antibodies Tuj (1:500, Covance) for general axon growth, GFAP (1:1000, Chemicon) for glial scar formation, and CGRP (1:2000, Peninsula) for sensory axons. These sections were incubated in primary antibodies overnight at room temperature followed by incubating in species-specific secondary antibodies (goat anti-mouse, donkey anti-goat, or goat anti-rabbit conjugated to FITC or rhodamine, 1:1000, Jackson ImmunoResearch) for 2 h at room temperature. Sections were coverslipped with fluoromount-G with DAPI (SouthernBiotech).

#### 2.11. Confocal microscopy

Immunohistological sections of the bovine spinal cord (thickness: 20  $\mu m)$  were imaged on a Nikon A1 laser scanning confocal microscope to generate z-stacks (approximately 10 slices with a 2- $\mu m$  step size) in the Nikon Elements software. Image quantification was performed by normalizing the intensity of either myelin or laminin stains within 100  $\times$  100  $\mu m^2$  measured areas. A macro in FIJI was written to automate image processing and quantification over the directory of images. Specifically the Huang Dark method was used to identify the stain-positive

region to quantify the protein of interest and normalized against the total area of the section measured. Cell nuclei quantification was conducted using moments dark thresholding followed by water shedding to separate the nuclei. Particle analysis was used to count nuclei with diameters of 5–10 μm with a circularity greater than 0.75. The number of cell nuclei was normalized to the area of each scan (1 mm<sup>2</sup>). Myelin and laminin quantification was performed by normalizing the intensity of stains within 1 mm<sup>2</sup> measured areas. For transplantation analysis, at least four adjacent sections on each slide (approximately 360  $\mu m$  in height) from each animal were scanned and analyzed. A 4X objective was used to provide lower magnification images to observe whether axons infiltrated through the rostral end and extended towards the caudal end. 10X and 20X objectives were used to quantify the number of infiltrating axons through the prefabricated channels in the scaffolds. Tuj + axons and CGRP fibers inside the scaffolds were quantified using the multi-point tool in ImageJ. Infiltration distance was analyzed using the measure tool in ImageJ.

#### 2.12. Statistics

One-way ANOVA and post-hoc Tukey's HSD tests were performed to calculate statistical significance unless stated otherwise. Statistical analysis of mechanical heterogeneity was calculated using a Welch Two Sample *t*-test, assuming normal distributions with unequal variances between groups between the gray and white matter of the scaffolds. Significant differences were denoted with p-values less than 0.05. In vivo analysis (9 animals total) was averaged from 3 histological sections per animal. Three different bovine spinal cords with three sections from each level (cervical, lumbar and sacral) were examined for rheology,

tensiometry and atomic force microscopy (AFM). Regarding the tensiometer and AFM experiments, at least 5 measurements were recorded from both the gray and white matter and 3 sections from each level were examined on the rheometer.

#### 3. Results

I. Microstructural characterization of spinal cord mechanical properties

In order to examine the heterogeneity of spinal cord tissue, initial experiments using AFM and tensiometry were conducted to interrogate differences in gray and white matter along the transverse anatomical plane. Previous experiments have found that the gray matter is stiffer than white matter in all anatomical planes (coronal, sagittal and transverse) [45], though there is also conflicting evidence of a significant difference between gray and white matter [8]. To clarify the discrepancies between these studies, AFM and tensiometry experiments were performed on bovine spinal cord (Fig. 1A and B). The tissue was divided into three regions: sacral, thoracic/lumbar, and cervical to assess whether anatomical level affected the mechanical properties of the cord. AFM, which has been used previously to characterize cord mechanics [49], revealed that the gray matter exhibits significant higher elastic moduli compared to white matter, though there were no statistical differences between the three levels for either region (Fig. 1C). Post-hoc Tukey tests indicated significant differences between gray and white matter at each level. Tensiometry examined the relaxation factors of both gray and white matter by measuring stress relaxation following indentation. Fig. 1D shows the relaxation factors for both gray and white

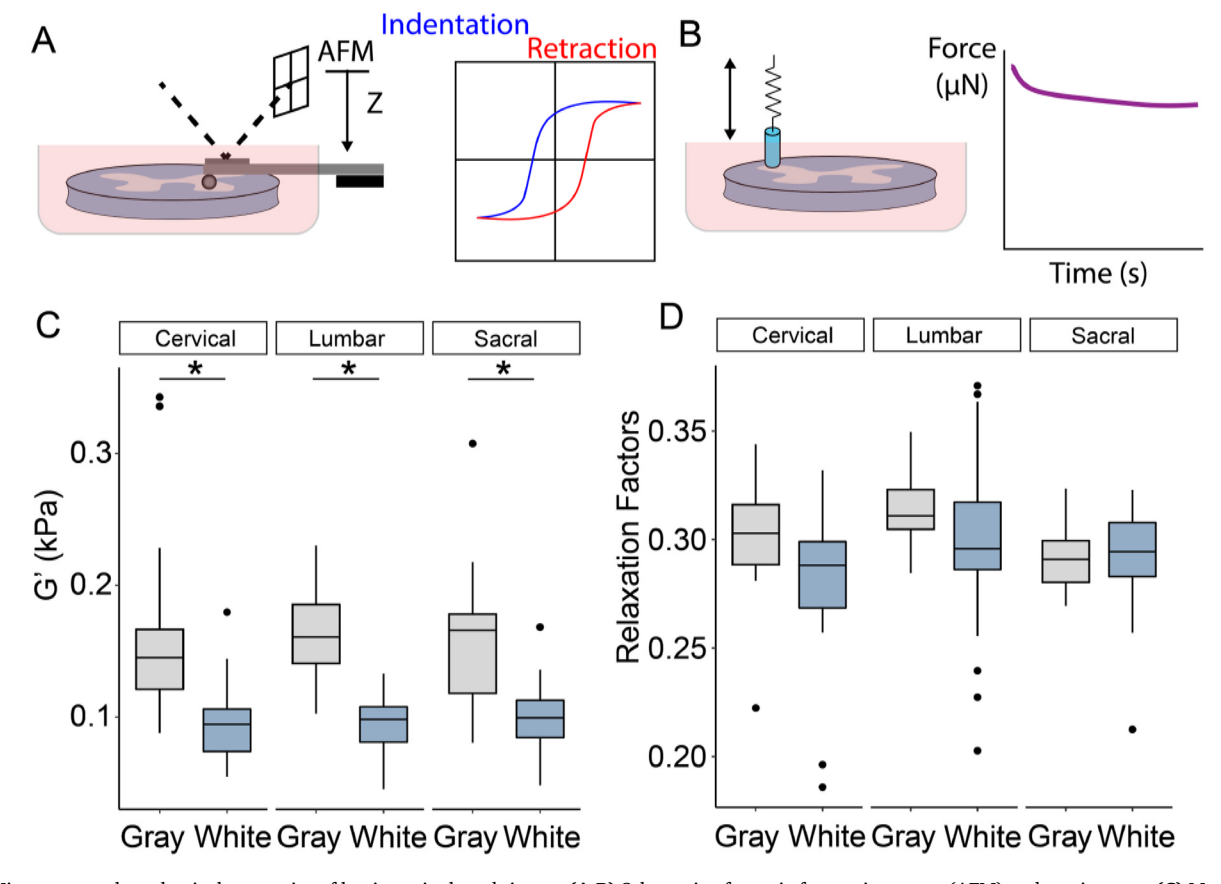


Fig. 1. Microstructural mechanical properties of bovine spinal cord tissues. (A,B) Schematic of atomic force microscopy (AFM) and tensiometer. (C) Measurements of gray and white matter using AFM. (D) Relaxation factors of gray and white matter via tensiometer. The box plots depict the median, 25 and 75 percentiles, and the whiskers represent 1.5x the interquartile range. \*p 0.05 (n = 5 measurements per matter with 3 sections from each level: cervical, lumbar, and sacral stemming from 3 animals).

K.A. Tran et al. Biomaterials 295 (2023) 122061

matter in all three regions, and two-factor ANOVAs revealed a statistical difference between the gray and white matter, though again there was no difference between levels. Taken together, these results indicated that the gray matter exhibited stiffer and more viscoelastic mechanics compared to white matter, and that there was no difference in the microstructural mechanical properties of gray and white matter along the length of the cord. To verify that this mechanical heterogeneity also exists within the rat spinal cord, AFM was conducted on cervical level slices of the rat cord and indicated a significantly higher elastic modulus in the gray matter region compared to the surrounding white matter region (Supplemental Fig. 1).

#### II. Macrostructural mechanical properties of spinal cord tissue

Rheology was conducted to characterize bulk mechanics of the cord at cervical, lumbar, and sacral levels. Three different sections from each level (cervical, lumbar and sacral) from three separate bovine spinal cords were examined with rheology (nine total samples). Given the results of the AFM testing, these experiments tested the hypothesis that the disparity in bulk mechanical properties of anatomical levels is due to differences in the ratio of gray-to-white matter. Therefore, shear storage and loss moduli as well as cross-sectional area of gray and white matter were measured in 5-6-mm thick transverse spinal cord sections taken from different levels. Fig. 2A–C shows rheological experiments

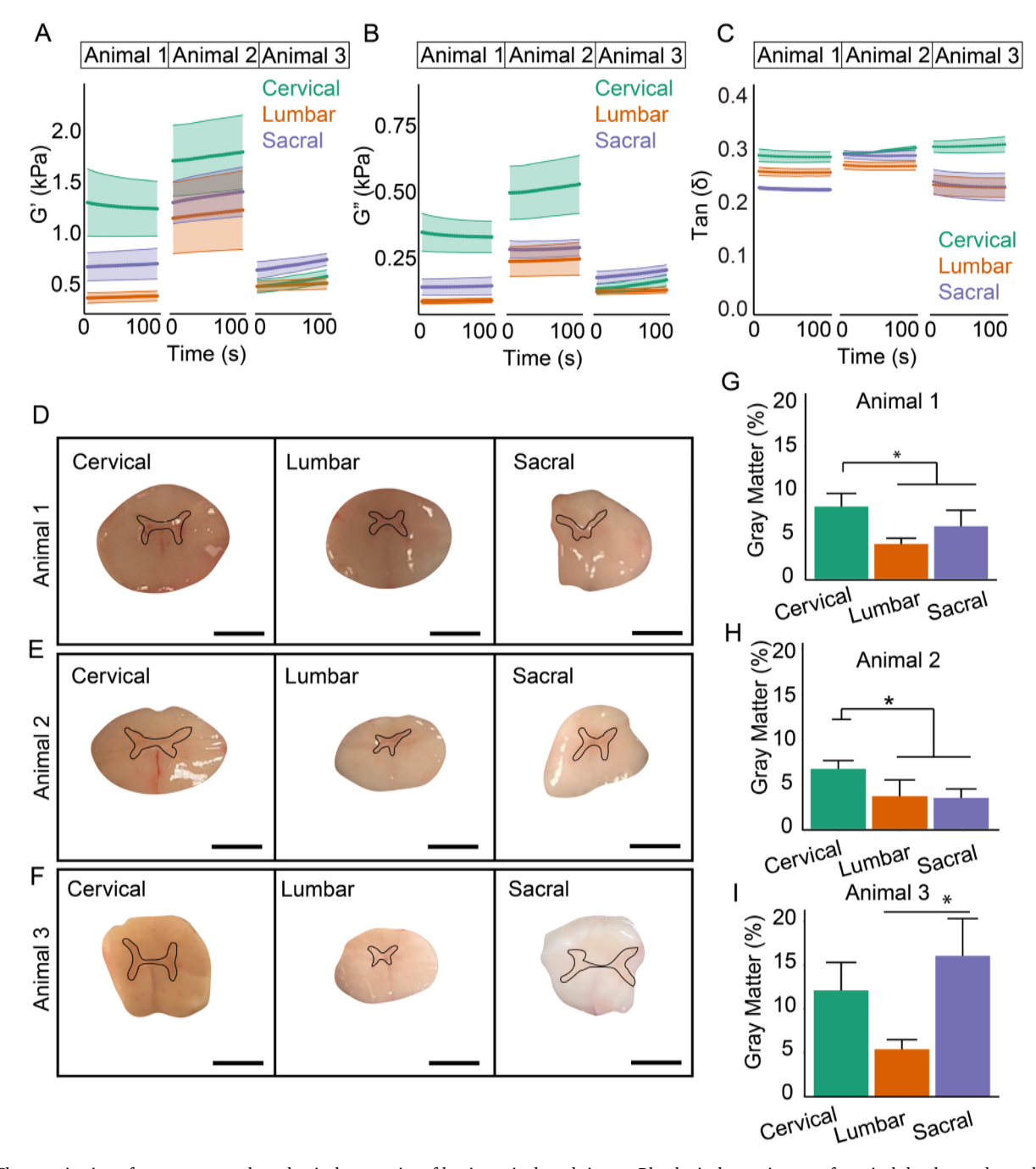


Fig. 2. Characterization of macrostructural mechanical properties of bovine spinal cord tissues. Rheological experiments of cervical, lumbar and sacral regions of spinal cords from 3 animals showing (A) storage modulus, (B) loss modulus and (C)  $\tan(\delta)$ . Data presented as mean  $\pm$  s.e.m. (D–F) Images of spinal cords and (G–I) quantification of gray-to-white matter ratios for each animal. The black lines indicate the representative regions of quantified gray matter. Data presented as mean  $\pm$  s.d. \*p 0.05 (n = 3 spinal sections from per level: cervical, lumbar, and sacral stemming from 3 animals).

performed on three different bovine spinal cords. The highest storage and loss moduli were measured in cervical regions of two of the animals and in the sacral region in the third animal. Moreover, Supplemental Fig. 2 displays the sections were tested at increasing magnitudes of compressive strain to demonstrate that the cord exhibited the compression stiffening observed in other tissues [50,51]. In order to reconcile the bulk testing with the AFM measurements that found no difference in gray or white matter along the cord, transverse spinal cord sections (Fig. 2D-F) were imaged and the percentage of gray matter in the cross-section was expressed as a percentage of the total area (Fig. 2G-I). Fig. 2G provides the rheological measurements for animal 1, Fig. 2H corresponds to animal 2 and Fig. 2I represents the data from animal 3 (all measurements were performed in triplicate). The gray matter in the cervical region was significantly higher compared to the lumbar and sacral regions in the experiment from the first two cords, and highest in the sacral region in the third animal. Therefore, these results suggested that bulk rheological properties along the cord were determined by differences in the ratio of gray to white matter in the cross-section of the cord, not the anatomical level.

#### III. Microstructural analysis of gray and white matter

In order to provide insight into structural differences between gray and white matter that give rise to mechanical heterogeneity, immunohistochemistry was performed to examine differences in cell nuclei, myelin, and laminin expression in both regions along the different levels of the cord. These measurements also provided an opportunity to assess whether the cords undergo substantial demyelination or changes in matrix content over the course of the mechanical experiments. Fig. 3 shows cervical, lumbar, and sacral sections fixed at the beginning (Fig. 3A,C,E) and 6 h later at the end (Fig. 3B,D,F) of the mechanical characterization experiments. Quantification of DAPI, myelin, and laminin indicated significant differences between the white and gray matter regions at all the levels. There was significantly higher DAPI staining in gray compared to white matter at both the beginning and end of the experiment (Fig. 3G), which is consistent with the results of a previous study [45]. Myelin and laminin also exhibited a higher intensity in the gray matter (Fig. 3H and I). In the white matter, the laminin-positive regions revealed a network pattern that may highlight the vascular bed, due to the prevalence of laminin in the basement membrane. The gray matter appeared much denser in both the myelin and laminin staining. Importantly, there was no significant difference between DAPI staining nor expression of myelin and laminin at the beginning of the experiment compared to the end of the experiment, verifying that the tissue did not undergo substantial degradation during the mechanical testing.

#### IV. 3D-printing scaffolds with heterogeneous mechanical properties

A novel DLP approach was developed to fabricate a scaffold that mimicked the difference in stiffness between gray and white regions observed by microstructural mechanical testing of the bovine spinal

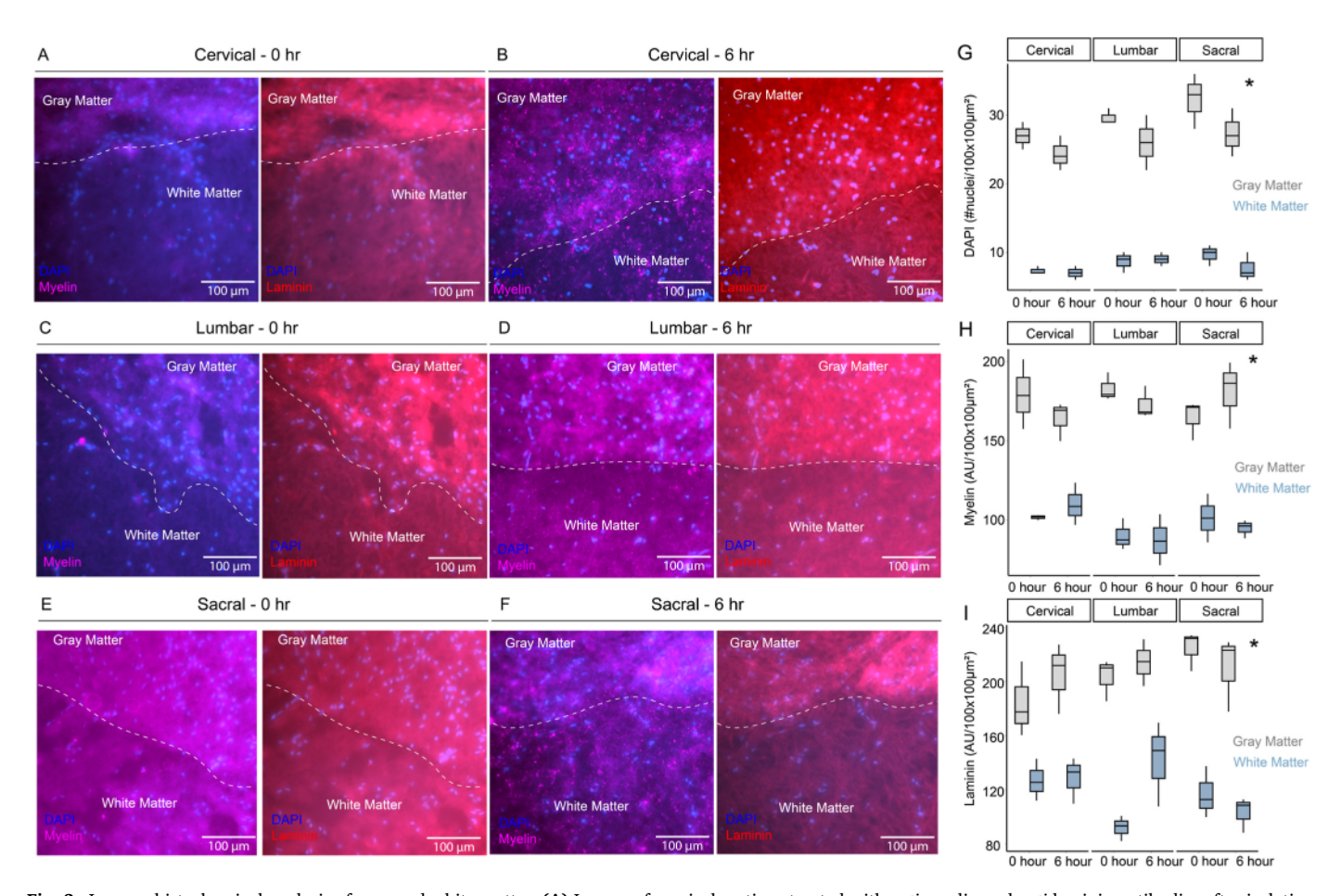


Fig. 3. Immunohistochemical analysis of gray and white matter. (A) Images of cervical sections treated with *anti*-myelin and *anti*-laminin antibodies after isolation and (B) at a 6-h time point. (C) Images of lumbar sections treated with anti-myelin and *anti*-laminin antibodies after isolation and (D) at a 6-h time point. (E) Images of sacral sections treated with anti-myelin and *anti*-laminin antibodies after isolation and (F) at a 6-h time point. Quantification of DAPI (G), myelin (H), and laminin (I) within the gray and white matter at both the beginning and end of experiment for all cord levels. The box plots depict the median, 25 and 75 percentiles, and the whiskers represent 1.5x the interquartile range. \*p 0.05 (n = 3 measurements per matter with 3 sections from each region: cervical, lumbar, and sacral at each time point).

cord. Fig. 4A shows a schematic of the printing method, which applied varying levels of light intensity to a single z-plane using a grayscale mask. Grayscale patterns were created to alter light intensity values between 0 and 100%, representing black to white, to modulate the extent of polymerization of the GelMA hydrogel. In order to verify this approach, test patterns of alternating intensity were printed in square blocks. Fig. 4B shows the grayscale mask used for these preliminary prints, with stripes of 1-mm thickness in a 10 x 10 x 3-mm block. Tensiometry was used to validate differences in mechanical properties. Quantification of this data and subsequent statistical analysis revealed significant differences between each stripe, demonstrating that the regions exposed to higher light intensities exhibited stiffer mechanics than the regions with lower light intensities (Fig. 4C). These results verified that heterogeneity can be achieved within the 3D-printed scaffolds to mimic the difference in stiffness between gray and white matter regions.

#### W. Mechanical characterization of 3D-printed scaffolds for spinal cord injury

Having validated the approach to 3D-print scaffolds with heterogeneous mechanical properties, hydrogels were printed to mimic a rat T10 geometry. Homogenous scaffolds were exposed with the same light intensity across the entire cross-section in both the "gray" and "white" regions, while heterogeneous scaffolds were printed with different intensity light between the two regions. Mechanical and microstructural assays were conducted to characterize these scaffolds. Previous studies have shown that the stiffening effect in photocrosslinkable hydrogels decreases dextran diffusivity [52], with the porosity of these scaffolds examined using a scanning electron microscope (SEM). Fig. 5A displays images of the scaffold within the gray and white matter regions in a homogenous scaffold (printed at the same light intensity used for the white matter of the heterogeneous scaffold) and one heterogeneous

scaffold. Quantification demonstrated that the pore diameters were decreased in the simulated gray matter of the heterogeneous scaffold (Fig. 5B), which is consistent with a previous study on modifying GelMA with altered light intensity [53]. In order to further validate the difference between simulated white and gray matter, compression tests were performed on bulk hydrogels exposed to varying light intensity. Compression tests revealed that hydrogels exposed to the light intensity used to create the gray matter region exhibited a significantly higher elastic modulus compared to hydrogels representing white matter (Fig. 5C). Nonetheless, the compression indicated no significant difference in the Poisson ratio of the hydrogels: both white and gray matter were nearly incompressible ( $\nu \sim 0.4$ ) (Fig. 5D). Having validated that there was a difference between the mechanical properties of scaffolds exposed to different pixel intensities, images of the homogeneous and heterogenous scaffolds were obtained to demonstrate that the varying stiffness did not affect the geometry of the scaffold (Fig. 5E). The scaffolds contained cylindrical channels with diameters of 325 µm to guide axonal infiltration into the scaffold due to their established ability to align axons along the rostral-caudal direction [16,42]. AFM raster scans were performed on the scaffold surface to provide two-dimensional elasticity maps. Three different printing conditions were used: homogenous stiffness printed at 75% intensity (simulated white matter), homogenous stiffness printed at 100% intensity (simulated gray matter), and heterogenous stiffness with varying light intensity in the gray and white regions. Fig. 5F-H displays heatmaps of the elastic moduli in both the homogeneous and heterogeneous scaffolds. Two-factor ANOVAs with post-hoc Tukey tests revealed that the gray matter within the heterogeneous scaffolds exhibited significantly higher elastic moduli than the surrounding white matter and the homogeneous hydrogels printed at 75% intensity. There was no significant difference between the stiffness of the gray matter in the heterogeneous scaffolds and the homogeneous scaffolds printed at 100% intensity (Fig. 5I). Taken

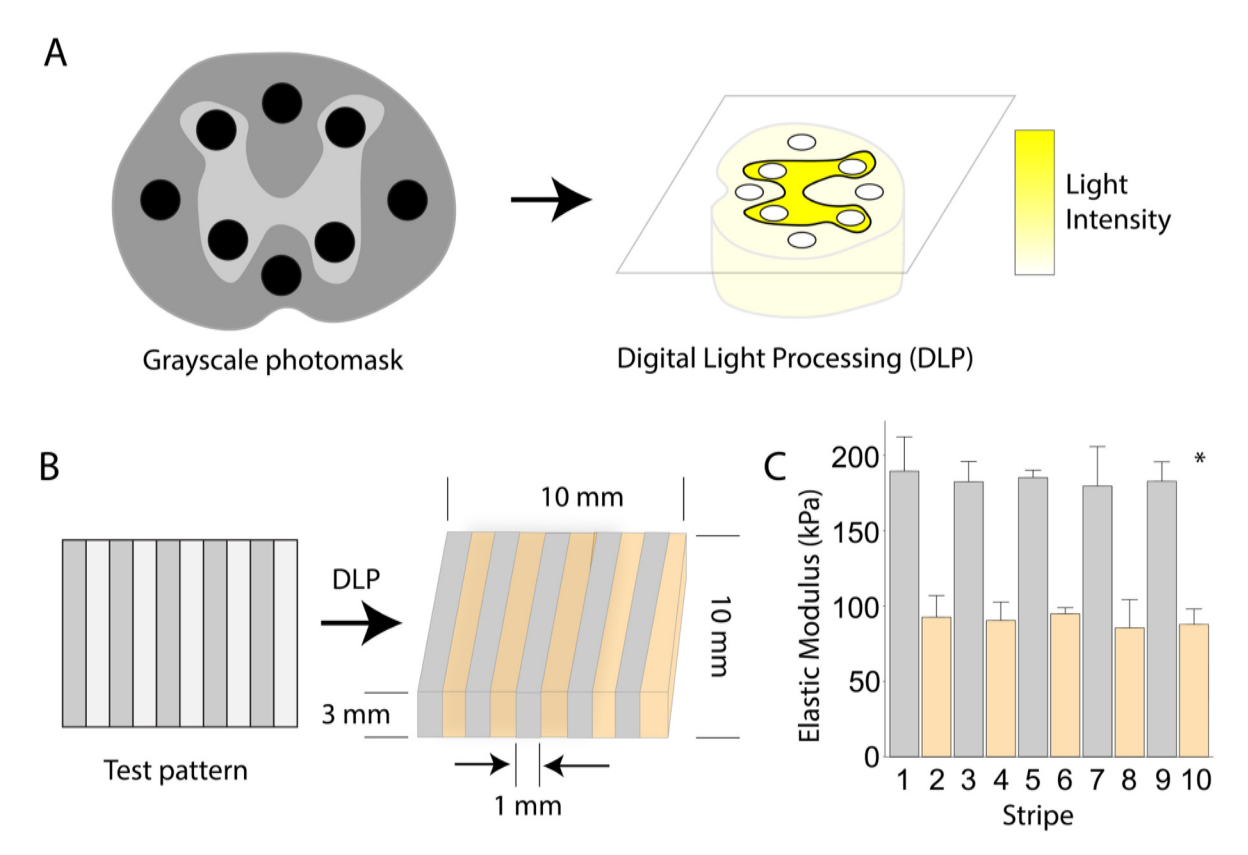


Fig. 4. 3D-printing scaffolds with heterogeneity. (A) Schematic of grayscale patterns to facilitate printing of a single plane with varying levels of light intensity. (B) Preliminary 3D-printed hydrogels with heterogeneity by using a mask with alternating light intensity. (C) Mechanical quantification of each stripe within the 3D-printed hydrogels. Data presented as mean  $\pm$  s.d. \*p 0.05 (n = 3, one measurement per stripe from 3 different gels).

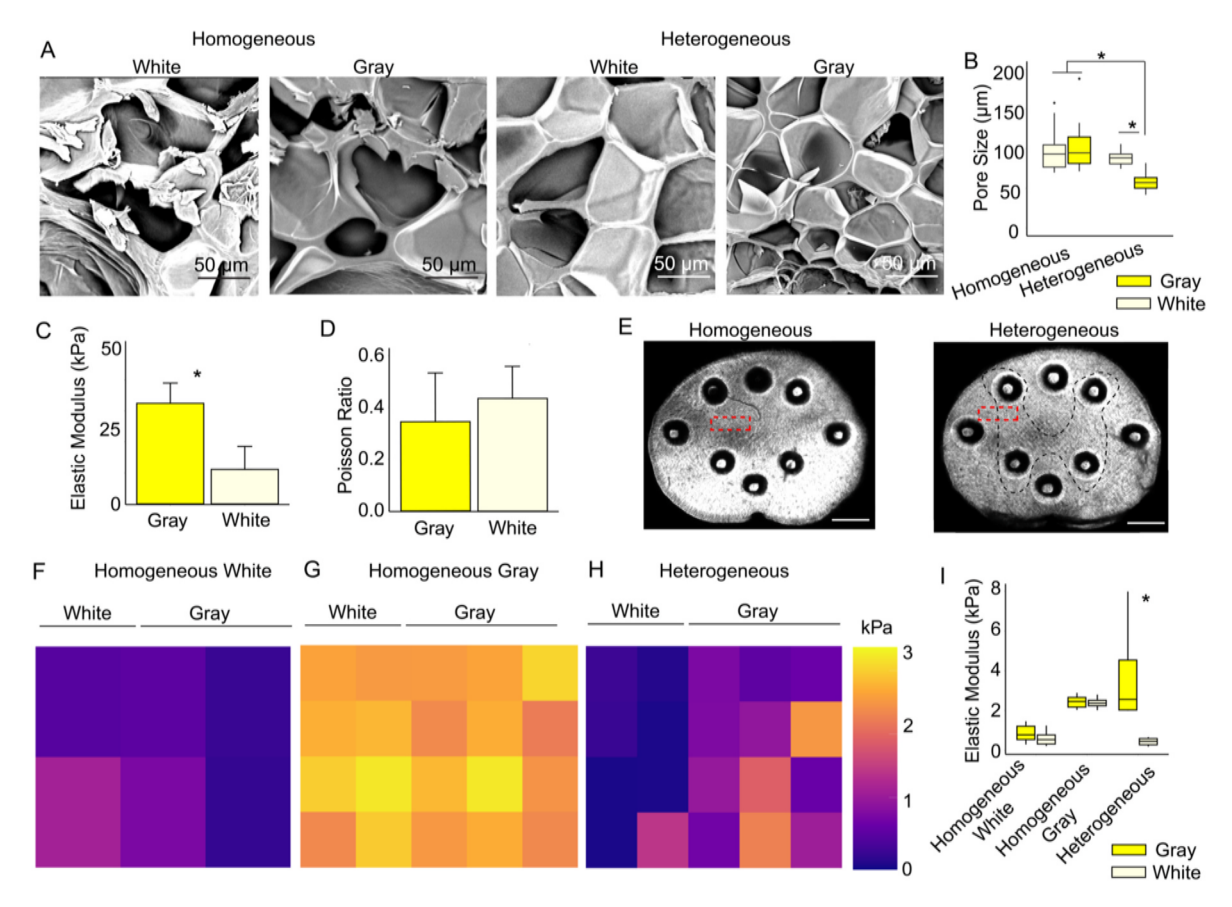


Fig. 5. Interrogation of 3D-printed heterogeneous scaffolds. (A) SEM images of the gray and white matter in homogeneous and heterogeneous hydrogels. (B) Quantification of porosity within the scaffolds. (C) Mechanical testing of 3D-printed scaffolds that exhibit the mechanics of gray matter and white matter. (D) Poisson ratios of 3D-printed scaffolds. (E) Brightfield images of 3D-printed scaffolds that mimic the T10 level of rat's spinal cord and exhibit homogeneous or heterogeneous mechanics within the constructs. Elasticity heatmaps of homogeneous white (F), homogeneous gray (G) and heterogeneous (H) scaffolds. (I) Young's moduli in both the gray and white matter within homogeneous and heterogeneous hydrogels. The data in the bar graphs are represented as mean  $\pm$  s.d. The box plots depict the median, 25 and 75 percentiles, and the whiskers represent 1.5x the interquartile range. Scale  $= 500 \, \mu m^* p$  0.05 (n = 3 scaffolds with at least 6 measurements from each matter).

together, this data demonstrated that mechanical heterogeneity can be achieved in spinal cord scaffolds.

### VI. Assessing axon infiltration into scaffolds with heterogeneous mechanical properties

Transplantation studies were then conducted to determine whether the heterogeneous scaffolds would elicit increased axon infiltration compared to homogeneous controls. Both heterogeneous scaffolds and homogeneous scaffolds of stiffnesses matching the heterogeneous scaffold were transplanted into a model of acute spinal cord injury. Fig. 6A displays a schematic of hydrogel fabrication, injury model, and transplantation of the T10 scaffolds. Immunohistochemistry examined the infiltration of axons into the channels patterned in the scaffold two weeks post-transplantation. The presence of ascending sensory-specific tracts was measured using calcitonin gene-related peptide (CGRP), a peptide widely expressed in sensory axons [54] (Fig. 6B). Quantification of CGRP<sup>+</sup> fibers demonstrated that heterogeneous scaffolds significantly augmented the infiltration of sensory axons compared to both homogeneous conditions (Fig. 6C). To further assess axon infiltration into the scaffolds, both the rostral and caudal regions of the transplanted scaffolds were examined for the presence of beta-tubulin III (Tuj) fibers. Fig. 6D displays the presence of Tuj<sup>+</sup> axons located only in the rostral region of the scaffolds with homogeneous mechanics matching the "white matter" of the heterogeneous scaffold. Fig. 6E indicates a similar response in the homogeneous scaffold matching the gray matter.

However, the infiltration and outgrowth of Tuj<sup>+</sup> fibers were observed in both the rostral and caudal sections of the heterogeneous scaffolds (Fig. 6F), demonstrating that the mechanical heterogeneity stimulated neuronal regeneration. In order to determine whether the heterogeneous scaffold stimulated increased axon growth, quantification of Tuj fibers was evaluated in the white matter regions of both scaffold types and indicated that the heterogeneous scaffolds significantly promoted the growth of Tuj+ fibers (Fig. 6G) and stimulated the infiltration distance compared to the homogeneous hydrogels (Fig. 6H). The heterogeneous scaffolds also exhibited increased infiltration of motor specific (5-HT+) and regenerating (RT-97+) axons compared to homogeneous controls (Supplemental Fig. 3). The scar area, as indicated by GFAP positive regions, was not substantially different between conditions (Supplemental Fig. 4). Overall, these results demonstrate 3D-printed scaffolds with heterogeneous mechanical properties matching the anisotropy of host tissue have beneficial effects on the infiltration and regrowth of axons.

#### 4. Discussion

The results demonstrate that mimicking the stiffness disparity between gray and white matter in an implantable scaffold encourages axon growth at the site of a rat spinal cord transection injury. Previous studies have demonstrated that multicellular migration is enhanced along a gradient in the rigidity of the extracellular matrix, referred to as durotaxis, in both in vivo [55] and in vitro [56,57] microenvironments. In

K.A. Tran et al. Biomaterials 295 (2023) 122061

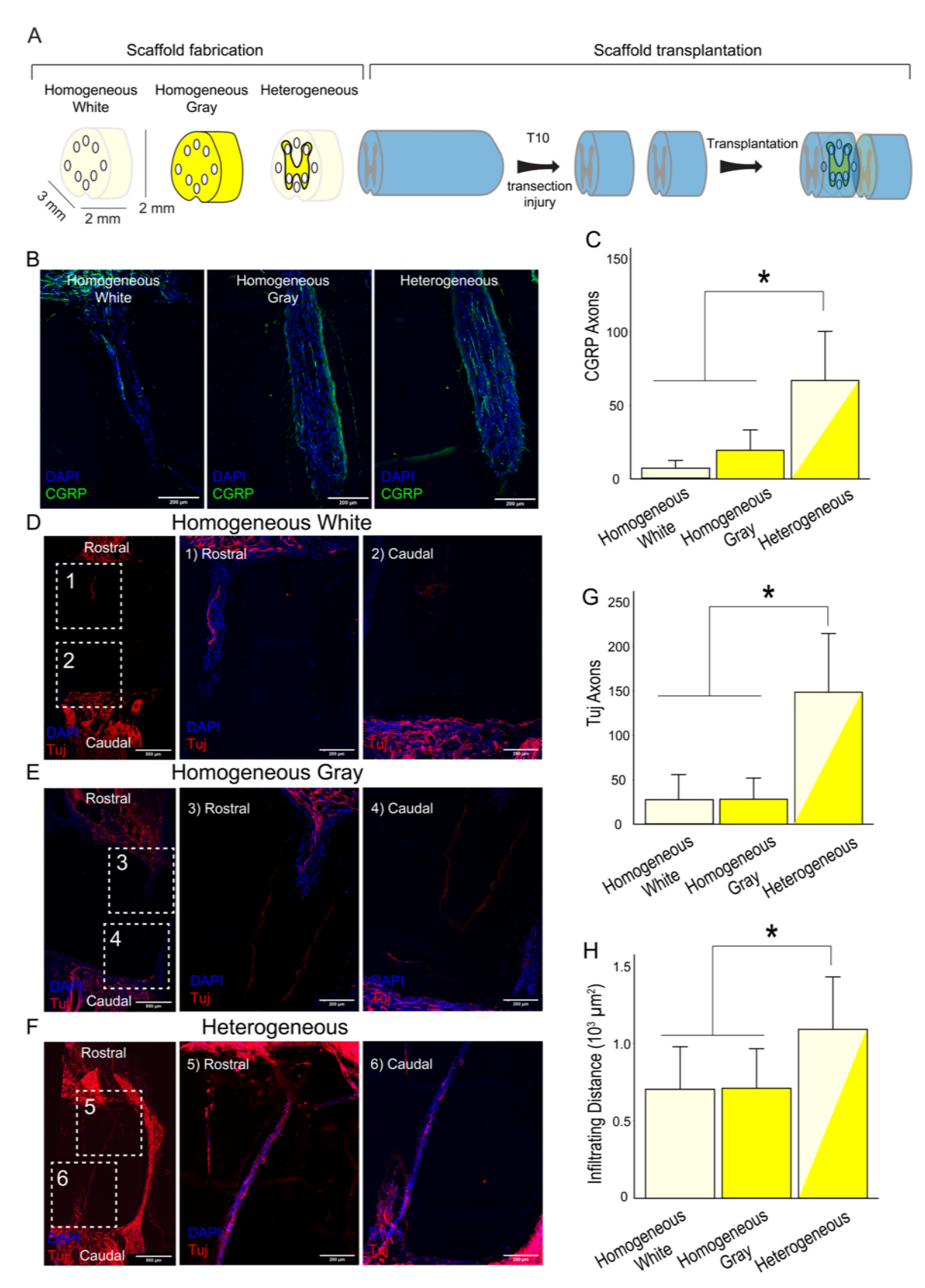


Fig. 6. Examination of axon infiltration post-transplantation. (A) Schematic showing scaffold fabrication to transplantation. (B,C) Immunofluorescence and quantification of CGRP<sup>+</sup> axons infiltrating the channels of both the homogeneous and heterogeneous scaffolds. (D,E,F) Infiltration of Tuj<sup>+</sup> fibers within the cylindrical channels in three scaffold conditions. Quantification of (G) Tuj + fibers and (H) infiltrating distance in homogeneous and heterogeneous scaffolds. The data in the bar graphs are represented as mean  $\pm$  s.d. \*p 0.05 (n = 3 histological slides for each condition).

contrast, the stiffness gradient used here is orthogonal to the direction of axonal growth, though this gradient is more representative of native spinal cord tissue. The mechanical testing conducted in this study indicates that the inner gray matter is stiffer than the surrounding white matter in the cord, and the mechanics of gray and white matter do not change along the rostral-caudal axis. The primary goal of a spinal cord scaffold or conduit is to encourage axon growth in the rostral-caudal direction to restore connectivity across the site of injury, since axon tracts are primarily aligned in this direction [14,25,42]. Therefore, the axons infiltrating the scaffold are not growing along a rigidity gradient, but like axon tracts in native tissue, they are growing in the rostral-caudal direction that is perpendicular to a disparity in matrix stiffness. The heterogeneity in scaffold stiffness may also affect the infiltration of other cell types beyond neurons including glial, immune, and vascular cells that may contribute to differences in axon infiltration. Overall, the mechanisms underlying increased axon infiltration in heterogeneous scaffolds compared to homogenous controls are likely different than those identified in previous durotaxis studies, including specific cell-matrix interactions [58,59] and small GTPase-mediated actomyosin contractility [60-62]. Future studies, which may include in vitro models of the spinal cord microenvironment, are therefore required to understand the molecular mechanisms responsible for the increased axon growth into the heterogeneous scaffolds.

The modification to digital light processing described here enables 3D-printing of complex topologies within mechanically heterogeneous hydrogels. DLP is a powerful tool for recreating complex tissue architectures in hydrogels, though previously the method has been limited to printing scaffolds exhibiting homogenous mechanics. However, other existing 3D-printing approaches are capable of printing interfacial and heterogeneous structures. For example, extrusion-based methods have been used to create heterogeneous aortic valve scaffolds [63]. But these methods are not applicable to softer, cell-permeable hydrogels, which are more appropriate for printing scaffolds with mechanics that match soft tissue like the spinal cord. And although 3D-printed scaffolds with elastic moduli greater than 200 kPa have been implanted within the spinal cord and demonstrated axon infiltration [42], DLP can recreate native tissue topology while also incorporating cell-based therapies by creating cell-permeable scaffolds with elastic moduli less than 10 kPa. One potential consideration for printing low stiffness hydrogels that is not addressed in this study is its effect on degradation rate and whether heterogeneous stiffness vields differences in degradation between the white and gray matter regions. Regardless of how the scaffolds are remodeled or degraded over time, the results of this study demonstrate that the initial stiffness gradient patterned in the heterogeneous scaffolds leads to increased axon infiltration at the 2-week time point. Moreover, the findings suggest that advancing DLP technology to print hydrogels with spatially varying mechanics provides an avenue to mimic the anisotropy of native tissues and to harness durotaxis by fabricating hydrogels that control cell growth and migration with stiffness gradients.

As advances in 3D-printing technology are made to mimic native tissue, one limitation to fabricating scaffolds that recreate the in vivo microenvironment is our understanding of complex tissue mechanics. Tissue mechanical properties are a function of multiple length scales, creating heterogeneity that is difficult to characterize and then implement in 3D-printed constructs. In this study, a variety of mechanical testing, including rheology and atomic force microscopy, are used to characterize spinal cord tissue ex vivo. These studies indicate that the macroscale mechanical properties of the spinal cord change as a function of level. Although previous work has shown that the mechanics of the cord are different based on the type of sectioning (e.g. coronal, sagittal, or transverse) [45], these results are the first to find differences in mechanical properties along the cord. Combining macroscale with microscale mechanical testing indicates that although the bulk mechanics differ along the cord, the mechanics of white matter and gray matter remain consistent and gray matter is stiffer than white matter.

Therefore, the differences in rheological properties arise from differences in the percentage of gray matter in the coronal section and not intrinsic disparity between levels. These findings justify the DLP-based approach to fabricate scaffolds that recreate a stiffer inner region to mimic the difference in gray-white matter mechanics. However, one aspect of the spinal cord tissue mechanics that the scaffolds do not mimic is viscoelasticity: the GelMA scaffolds are primarily elastic even though tensiometry indicated that gray matter exhibited higher stress relaxation. Therefore, there is a need for photoinks with tunable viscoelasticity, especially for tissues like the spinal cord that exhibit these properties.

Nonetheless, the DLP approach described here has the flexibility to incorporate existing neurotrophic therapies. As mentioned, in contrast to other 3D-printing approaches, the GelMA scaffolds printed for these studies are compatible with cell seeding within the bulk of the scaffold. There are currently ongoing clinical trials evaluating the efficacy of intrathecal injection of mesenchymal stem cells (MSC) in spinal cord injury patients [64], with evidence that MSCs release neurotrophic factors to stimulate axon growth and connectivity. Therefore, future studies will interrogate the benefit of incorporating MSCs into the heterogeneous scaffolds following implantation at the site of injury. In contrast to intrathecal injection, this approach can augment the residence time for MSCs at the site of injury and determine whether longer retention is beneficial. Moreover, the composition of the scaffold is also tunable. Although GelMA is used here, the DLP approach is compatible with many photoinks. Therefore, printing heterogeneous mechanics in degradable [65] or electrically conductive [28] photoinks provides a new means to combine different aspects of regenerative approaches in a multifunctional scaffold that mimics the mechanical anisotropy of native tissue.

#### 5. Conclusions

The bulk rheological testing of transverse spinal cord sections reveals that the viscoelastic properties of the cord change along its length. But rather than being due to differences in microstructural properties, AFM and tensiometry indicate that the stiffness of gray and white matter does not change according to level. Therefore, the differences in bulk mechanical properties along the cord are caused by the disparity in the relative amounts of gray and white matter. A modification to an existing digital light processing technique that facilitates printing of scaffolds with heterogeneous mechanical properties provides a means to mimic the difference in stiffness between gray and white matter. Transplantation experiments in an acute transection rat model indicate that scaffolds featuring this heterogeneous mechanical profile result in greater axon infiltration compared to homogeneous mechanical properties. Although the mechanism underlying this difference is unclear, these results highlight the importance of developing biomaterials that mimic the spatial heterogeneity of spinal cord tissue.

#### Credit author statement

Kiet A. Tran: conceptualization, methodology, software, validation, formal analysis, investigation, resources, data curation, writing (original, draft, review & editing), and visualization, Brandon J. DeOre: methodology, software, formal analysis & investigation, David Ikejiani: methodology, software & investigation, Kristen Means: methodology, software & investigation, Louis S. Paone: methodology & investigation, Laura De Marchi: methodology & investigation, Łukasz Suprewicz: data curation, formal analysis & investigation, Katarina Koziol: methodology & investigation, Julien Bouyer: methodology & investigation, Fitzroy J. Byfield: methodology & investigation, Ying Jin: methodology & investigation, Penelope Georges: conceptualization & methodology, Itzhak Fischer: conceptualization, resources, & methodology, writing (review & editing), Peter A. Galie: conceptualization, methodology, investigation,

resources, writing (original, draft, review & editing), supervision.

#### Declaration of competing interest

The authors declare that they have no known competing financial interests or personal relationships that could have appeared to influence the work reported in this paper.

#### Data availability

Raw and processed data and files needed to print the scaffolds are accessible in the Harvard Dataverse Repository at the following link: https://dataverse.harvard.edu/dataverse/galielab.

#### Acknowledgments

We would like to thank Dr. Jordan Miller for helpful discussions and Kevin Jansen for assistance in printing scaffolds. We are especially grateful for the great people at Bringhurst Meats in Berlin, New Jersey for generously providing the bovine spinal cord tissue for the mechanical testing experiments. This work was funded by the Craig H. Neilsen Foundation (I.F. and P.A.G.), the National Science Foundation (Award ID: 2223318, P.A.G.), and the National Institutes of Health (Award ID: R35 GM136259, F.J.B. and P.A.J.).

#### Appendix A. Supplementary data

Supplementary data to this article can be found online at https://doi.org/10.1016/j.biomaterials.2023.122061.

#### References

- [1] M. Iwashita, N. Kataoka, K. Toida, Y. Kosodo, Systematic profiling of spatiotemporal tissue and cellular stiffness in the developing brain, Development 141 (2014) 3793–3798, https://doi.org/10.1242/dev.109637.
- [2] B.S. Elkin, E.U. Azeloglu, K.D. Costa, B. Morrison III, Mechanical heterogeneity of the rat Hippocampus measured by atomic force microscope indentation, J. Neurotrauma 24 (2007) 812–822, https://doi.org/10.1089/neu.2006.0169.
- [3] A.F. Christ, K. Franze, H. Gautier, P. Moshayedi, J. Fawcett, R.J.M. Franklin, R. T. Karadottir, J. Guck, Mechanical difference between white and gray matter in the rat cerebellum measured by scanning force microscopy, J. Biomech. 43 (2010) 2986–2992, https://doi.org/10.1016/j.jbiomech.2010.07.002.
- [4] S. Chatelin, A. Constantinesco, R. Willinger, Fifty years of brain tissue mechanical testing: from in vitro to in vivo investigations, Biorheology 47 (2010) 255–276, https://doi.org/10.3233/BIR-2010-0576.
- [5] S. Cheng, E.C. Clarke, L.E. Bilston, Rheological properties of the tissues of the central nervous system: a review, Med. Eng. Phys. 30 (2008) 1318–1337, https:// doi.org/10.1016/j.medengphy.2008.06.003.
- [6] A. di Ieva, F. Grizzi, E. Rognone, Z.T.H. Tse, T. Parittotokkaporn, F. Rodriguez y Baena, M. Tschabitscher, C. Matula, S. Trattnig, R. Rodriguez y Baena, Magnetic resonance elastography: a general overview of its current and future applications in brain imaging, Neurosurg. Rev. 33 (2010) 137–145, https://doi.org/10.1007/s10143-010-0249-6.
- [7] Y.K. Mariappan, K.J. Glaser, R.L. Ehman, Magnetic resonance elastography: a review, Clin. Anat. 23 (2010) 497–511, https://doi.org/10.1002/ca.21006.
- [8] K. Ichihara, T. Taguchi, Y. Shimada, I. Sakuramoto, S. Kawano, S. Kawai, Gray matter of the bovine cervical spinal cord is mechanically more rigid and fragile than the white matter, J. Neurotrauma 18 (2001) 361–367, https://doi.org/ 10.1089/08977150151071053.
- T.-K. Hung, G.-L. Chang, J.-L. Chang, M.S. Albin, Stress-strain relationship and neurological sequelae of uniaxial elongation of the spinal cord of cats, Surg. Neurol. 15 (1981) 471–476, https://doi.org/10.1016/S0090-3019(81)80043-2.
- [10] L.E. Bilston, L.E. Thibault, The mechanical properties of the human cervical spinal cordin Vitro, Ann. Biomed. Eng. 24 (1995) 67–74, https://doi.org/10.1007/ BF02770996.
- [11] E. Moeendarbary, I.P. Weber, G.K. Sheridan, D.E. Koser, S. Soleman, B. Haenzi, E. J. Bradbury, J. Fawcett, K. Franze, The soft mechanical signature of glial scars in the central nervous system, Nat. Commun. 8 (2017) 1–11, https://doi.org/10.1038/ncomms14787.
- [12] J.M. Massey, J. Amps, M.S. Viapiano, R.T. Matthews, M.R. Wagoner, C. M. Whitaker, W. Alilain, A.L. Yonkof, A. Khalyfa, N.G.F. Cooper, J. Silver, S. M. Onifer, Increased chondroitin sulfate proteoglycan expression in denervated brainstem targets following spinal cord injury creates a barrier to axonal regeneration overcome by chondroitinase ABC and neurotrophin-3, Exp. Neurol. 209 (2008) 426–445, https://doi.org/10.1016/j.expneurol.2007.03.029.

- [13] Y.-M. Yuan, C. He, The glial scar in spinal cord injury and repair, Neurosci. Bull. 29 (2013) 421–435, https://doi.org/10.1007/s12264-013-1358-3.
- [14] P.P. Partyka, Y. Jin, J. Bouyer, A. DaSilva, G.A. Godsey, R.G. Nagele, I. Fischer, P. A. Galie, Harnessing neurovascular interaction to guide axon growth, Sci. Rep. 9 (2019) 1–10, https://doi.org/10.1038/s41598-019-38558-y.
- [15] P.S. Donoghue, R. Lamond, S.D. Boomkamp, T. Sun, N. Gadegaard, M.O. Riehle, S. C. Barnett, The development of a e-polycaprolactone scaffold for central nervous system repair, Tissue Eng. 19 (2013) 497–507, https://doi.org/10.1089/ten.tea.2012.0382.
- [16] D. Shahriari, J.Y. Koffler, M.H. Tuszynski, W.M. Campana, J.S. Sakamoto, Hierarchically ordered porous and high-volume polycaprolactone microchannel scaffolds enhanced axon growth in transected spinal cords, Tissue Eng. 23 (2017) 415–425, https://doi.org/10.1089/ten.tea.2016.0378.
- [17] S. Zhang, X.-J. Wang, W.-S. Li, X.-L. Xu, J.-B. Hu, X.-Q. Kang, J. Qi, X.-Y. Ying, J. You, Y.-Z. Du, Polycaprolactone/polysialic acid hybrid, multifunctional nanofiber scaffolds for treatment of spinal cord injury, Acta Biomater. 77 (2018) 15–27, https://doi.org/10.1016/j.actbio.2018.06.038.
- [18] X. Zhou, G. Shi, B. Fan, X. Cheng, X. Zhang, X. Wang, S. Liu, Y. Hao, Z. Wei, L. Wang, S. Feng, Polycaprolactone electrospun fiber scaffold loaded with iPSCs-NSCs and ASCs as a novel tissue engineering scaffold for the treatment of spinal cord injury, Int. J. Nanomed. 13 (2018) 6265–6277, https://doi.org/10.2147/IJN. S175914.
- [19] X. Zhang, B. Gong, J. Zhai, Y. Zhao, Y. Lu, L. Zhang, J. Xue, A perspective: electrospun fibers for repairing spinal cord injury, Chem. Res. Chin. Univ. 37 (2021) 404–410, https://doi.org/10.1007/s40242-021-1162-y.
- [20] K. Xi, Y. Gu, J. Tang, H. Chen, Y. Xu, L. Wu, F. Cai, L. Deng, H. Yang, Q. Shi, W. Cui, L. Chen, Microenvironment-responsive immunoregulatory electrospun fibers for promoting nerve function recovery, Nat. Commun. 11 (2020) 4504, https://doi. org/10.1038/s41467-020-18265-3.
- [21] N.J. Schaub, C.D. Johnson, B. Cooper, R.J. Gilbert, Electrospun fibers for spinal cord injury research and regeneration, J. Neurotrauma 33 (2016) 1405–1415, https://doi.org/10.1089/neu.2015.4165.
- [22] Z. Yu, H. Li, P. Xia, W. Kong, Y. Chang, C. Fu, K. Wang, X. Yang, Z. Qi, Application of fibrin-based hydrogels for nerve protection and regeneration after spinal cord injury, J. Biol. Eng. 14 (2020) 22, https://doi.org/10.1186/s13036-020-00244-3.
- [23] Z. Zhang, S. Yao, S. Xie, X. Wang, F. Chang, J. Luo, J. Wang, J. Fu, Effect of hierarchically aligned fibrin hydrogel in regeneration of spinal cord injury demonstrated by tractography: a pilot study, Sci. Rep. 7 (2017), 40017, https:// doi.org/10.1038/srep40017.
- [24] T. Sudhadevi, H.S. Vijayakumar, E. v Hariharan, S. Sandhyamani, L.K. Krishnan, Optimizing fibrin hydrogel toward effective neural progenitor cell delivery in spinal cord injury, Biomed. Mater. 17 (2022), 014102, https://doi.org/10.1088/ 1748-605 Vas-6600
- [25] K.A. Tran, Y. Jin, J. Bouyer, B.J. DeOre, Ł. Suprewicz, A. Figel, H. Walens, I. Fischer, P.A. Galie, Magnetic alignment of injectable hydrogel scaffolds for spinal cord injury repair, Biomater. Sci. (2022), https://doi.org/10.1039/d1bm01590g.
- [26] K.A. Tran, P.P. Partyka, Y. Jin, J. Bouyer, I. Fischer, P.A. Galie, Vascularization of self-assembled peptide scaffolds for spinal cord injury repair, Acta Biomater. 104 (2020) 76–84, https://doi.org/10.1016/j.actbio.2019.12.033.
- [27] T. Nakahashi, H. Fujimura, C.A. Altar, J. Li, J.I. Kambayashi, N.N. Tandon, B. Sun, Vascular endothelial cells synthesize and secrete brain-derived neurotrophic factor, FEBS Lett. 470 (2000) 113–117, https://doi.org/10.1016/S0014-5793(00)01302-8
- [28] E.A. Kiyotake, E.E. Thomas, H.B. Homburg, C.K. Milton, A.D. Smitherman, N. D. Donahue, K. Fung, S. Wilhelm, M.D. Martin, M.S. Detamore, Conductive and injectable hyaluronic acid/gelatin/gold nanorod hydrogels for enhanced surgical translation and bioprinting, J. Biomed. Mater. Res. 110 (2022) 365–382, https://doi.org/10.1002/jbm.a.37294.
- [29] D. Shahriari, M. Shibayama, D.A. Lynam, K.J. Wolf, G. Kubota, J.Y. Koffler, M. H. Tuszynski, W.M. Campana, J.S. Sakamoto, Peripheral nerve growth within a hydrogel microchannel scaffold supported by a kink-resistant conduit, J. Biomed. Mater. Res. 105 (2017) 3392–3399, https://doi.org/10.1002/jbm.a.36186.
- [30] K.M. Pawelec, J. Koffler, D. Shahriari, A. Galvan, M.H. Tuszynski, J. Sakamoto, Microstructure and in vivo characterization of multi-channel nerve guidance scaffolds, Biomed. Mater. 13 (2018), 044104, https://doi.org/10.1088/1748-605X/aaad85.
- [31] A. Bakshi, O. Fisher, T. Dagci, B.T. Himes, I. Fischer, A. Lowman, Mechanically engineered hydrogel scaffolds for axonal growth and angiogenesis after transplantation in spinal cord injury, J. Neurosurg. Spine 1 (2004) 322–329, https://doi.org/10.3171/spi.2004.1.3.0322.
- [32] M. Costantini, S. Testa, E. Fornetti, A. Barbetta, M. Trombetta, S.M. Cannata, C. Gargioli, A. Rainer, Engineering muscle networks in 3D gelatin methacryloyl hydrogels: influence of mechanical stiffness and geometrical confinement, Front. Bioeng. Biotechnol. 5 (2017), https://doi.org/10.3389/fbioe.2017.00022.
- [33] J. Lewandowska-Łańcucka, K. Mystek, A. Mignon, S. van Vlierberghe, A. Łatkiewicz, M. Nowakowska, Alginate- and gelatin-based bioactive photocrosslinkable hybrid materials for bone tissue engineering, Carbohydr. Polym. 157 (2017) 1714–1722, https://doi.org/10.1016/j.carbpol.2016.11.051.
- [34] M.T. Poldervaart, B. Goversen, M. de Ruijter, A. Abbadessa, F.P.W. Melchels, F. C. Öner, W.J.A. Dhert, T. Vermonden, J. Alblas, 3D bioprinting of methacrylated hyaluronic acid (MeHA) hydrogel with intrinsic osteogenicity, PLoS One 12 (2017), e0177628, https://doi.org/10.1371/journal.pone.0177628.
- [35] Q. Feng, K. Wei, S. Lin, Z. Xu, Y. Sun, P. Shi, G. Li, L. Bian, Mechanically resilient, injectable, and bioadhesive supramolecular gelatin hydrogels crosslinked by weak host-guest interactions assist cell infiltration and in situ tissue regeneration,

- Biomaterials 101 (2016) 217–228, https://doi.org/10.1016/j.biomaterials.2016.05.043.
- [36] X. Li, S. Chen, J. Li, X. Wang, J. Zhang, N. Kawazoe, G. Chen, 3D culture of chondrocytes in gelatin hydrogels with different stiffness, Polymers 8 (2016) 269, https://doi.org/10.3390/polym8080269.
- [37] C. Chung, M. Beecham, R.L. Mauck, J.A. Burdick, The influence of degradation characteristics of hyaluronic acid hydrogels on in vitro neocartilage formation by mesenchymal stem cells, Biomaterials 30 (2009) 4287–4296, https://doi.org/ 10.1016/j.biomaterials.2009.04.040.
- [38] I.E. Erickson, A.H. Huang, C. Chung, R.T. Li, J.A. Burdick, R.L. Mauck, Differential maturation and structure–function relationships in mesenchymal stem cell- and chondrocyte-seeded hydrogels, Tissue Eng. 15 (2009) 1041–1052, https://doi.org/ 10.1089/ten.tea.2008.0099
- [39] S.J. Bryant, K.S. Anseth, The effects of scaffold thickness on tissue engineered cartilage in photocrosslinked poly(ethylene oxide) hydrogels, Biomaterials 22 (2001) 619–626, https://doi.org/10.1016/S0142-9612(00)00225-8.
- [40] H. Li, A.M. Koenig, P. Sloan, N.D. Leipzig, In vivo assessment of guided neural stem cell differentiation in growth factor immobilized chitosan-based hydrogel scaffolds, Biomaterials 35 (2014) 9049–9057, https://doi.org/10.1016/j. biomaterials 2014.07.032
- [41] N.D. Leipzig, R.G. Wylie, H. Kim, M.S. Shoichet, Differentiation of neural stem cells in three-dimensional growth factor-immobilized chitosan hydrogel scaffolds, Biomaterials 32 (2011) 57–64, https://doi.org/10.1016/j. biomaterials 2010 09 031
- [42] J. Koffler, W. Zhu, X. Qu, O. Platoshyn, J.N. Dulin, J. Brock, L. Graham, P. Lu, J. Sakamoto, M. Marsala, S. Chen, M.H. Tuszynski, Biomimetic 3D-printed scaffolds for spinal cord injury repair, Nat. Med. (2019), https://doi.org/10.1038/s41591.018.0206.7
- [43] B. Grigoryan, S.J. Paulsen, D.C. Corbett, D.W. Sazer, C.L. Fortin, A.J. Zaita, P. T. Greenfield, N.J. Calafat, J.P. Gounley, A.H. Ta, F. Johansson, A. Randles, J. E. Rosenkrantz, J.D. Louis-Rosenberg, P.A. Galie, K.R. Stevens, J.S. Miller, Multivascular networks and functional intravascular topologies within biocompatible hydrogels, Science 2019 (1979) 364, https://doi.org/10.1126/science.aav9750, 458–464.
- [44] I.S. Kinstlinger, J.S. Miller, 3D-printed fluidic networks as vasculature for engineered tissue, Lab Chip 16 (2016) 2025–2043, https://doi.org/10.1039/ C6LC00193A.
- [45] D.E. Koser, E. Moeendarbary, J. Hanne, S. Kuerten, K. Franze, CNS cell distribution and axon orientation determine local spinal cord mechanical properties, Biophys. J. 108 (2015) 2137–2147, https://doi.org/10.1016/j.bpj.2015.03.039.
- [46] P. Mitra, R.M. Brownstone, An in vitro spinal cord slice preparation for recording from lumbar motoneurons of the adult mouse, J. Neurophysiol. 107 (2012) 728–741, https://doi.org/10.1152/jn.00558.2011.
- [47] M. Richner, S.B. Jager, P. Siupka, C.B. Vaegter, Hydraulic extrusion of the spinal cord and isolation of dorsal root ganglia in rodents, JoVE (2017), https://doi.org/ 10.3701/55226
- [48] M. Griffin, R. Casadio, C.M. Bergamini, Transglutaminases: nature's biological glues, Biochem. J. 368 (2002) 377–396, https://doi.org/10.1042/bj20021234.
- [49] A. Domínguez-Bajo, A. González-Mayorga, C.R. Guerrero, F.J. Palomares, R. García, E. López-Dolado, M.C. Serrano, Myelinated axons and functional blood vessels populate mechanically compliant rGO foams in chronic cervical hemisected rats, Biomaterials 192 (2019) 461–474, https://doi.org/10.1016/j. biomaterials.2018.11.024.
- [50] K. Pogoda, L. Chin, P.C. Georges, F.J. Byfield, R. Bucki, R. Kim, M. Weaver, R. G. Wells, C. Marcinkiewicz, P.A. Janmey, Compression stiffening of brain and its effect on mechanosensing by glioma cells, New J. Phys. 16 (2014), 075002, https://doi.org/10.1088/1367-2630/16/7/075002.

- [51] M. Perepelyuk, L. Chin, X. Cao, A. van Oosten, V.B. Shenoy, P.A. Janmey, R. G. Wells, Normal and fibrotic rat livers demonstrate shear strain softening and compression stiffening: a model for soft tissue mechanics, PLoS One 11 (2016), e0146588, https://doi.org/10.1371/journal.pone.0146588.
- [52] L. Bian, C. Hou, E. Tous, R. Rai, R.L. Mauck, J.A. Burdick, The influence of hyaluronic acid hydrogel crosslinking density and macromolecular diffusivity on human MSC chondrogenesis and hypertrophy, Biomaterials 34 (2013) 413–421, https://doi.org/10.1016/j.biomaterials.2012.09.052.
- [53] C. Puckert, E. Tomaskovic-Crook, S. Gambhir, G.G. Wallace, J.M. Crook, M. J. Higgins, Electro-mechano responsive properties of gelatin methacrylate (GelMA) hydrogel on conducting polymer electrodes quantified using atomic force microscopy, Soft Matter 13 (2017) 4761–4772, https://doi.org/10.1039/C7SM00335H
- [54] X.Q. Li, V.M.K. Verge, J.M. Johnston, D.W. Zochodne, CGRP peptide and regenerating sensory axons, J. Neuropathol. Exp. Neurol. 63 (2004) 1092–1103, https://doi.org/10.1093/jnen/63.10.1092.
- [55] A. Shellard, R. Mayor, Collective durotaxis along a self-generated stiffness gradient in vivo, Nature 600 (2021) 690–694, https://doi.org/10.1038/s41586-021-04210-x.
- [56] I. Pi-Jauma, R. Alert, J. Casademunt, Collective durotaxis of cohesive cell clusters on a stiffness gradient, The European Physical Journal E 45 (2022) 7, https://doi. org/10.1140/epje/s10189-021-00150-6.
- [57] C.F. Guimarães, L. Gasperini, A.P. Marques, R.L. Reis, The stiffness of living tissues and its implications for tissue engineering, Nat. Rev. Mater. 5 (2020) 351–370, https://doi.org/10.1038/s41578-019-0169-1.
- [58] C.D. Hartman, B.C. Isenberg, S.G. Chua, J.Y. Wong, Vascular smooth muscle cell durotaxis depends on extracellular matrix composition, Proc. Natl. Acad. Sci. USA 113 (2016) 11190–11195, https://doi.org/10.1073/pnas.1611324113.
- [59] J.A. Espina, C.L. Marchant, E.H. Barriga, Durotaxis: the mechanical control of directed cell migration, FEBS J. 289 (2022) 2736–2754, https://doi.org/10.1111/ febs.15862.
- [60] B.J. DeOre, P.P. Partyka, F. Fan, P.A. Galie, CD44 mediates shear stress mechanotransduction in an in vitro blood-brain barrier model through small GTPases RhoA and Rac1, Faseb. J. 36 (2022), https://doi.org/10.1096/ fi.202100822RR.
- [61] B.J. DeOre, A. Baldwin-LeClair, K.A. Tran, A. DaSilva, F.J. Byfield, P.A. Janmey, P. A. Galie, Microindentation of fluid-filled cellular domes reveals the contribution of RhoA-ROCK signaling to multicellular mechanics, Small 18 (2022), 2200883, https://doi.org/10.1002/smll.202200883.
- [62] B.J. DeOre, K.A. Tran, A.M. Andrews, S.H. Ramirez, P.A. Galie, SARS-CoV-2 spike protein disrupts blood-brain barrier integrity via RhoA activation, J. Neuroimmune Pharmacol. 16 (2021) 722–728, https://doi.org/10.1007/ s11481-021-10029-0.
- [63] L.A. Hockaday, K.H. Kang, N.W. Colangelo, P.Y.C. Cheung, B. Duan, E. Malone, J. Wu, L.N. Girardi, L.J. Bonassar, H. Lipson, C.C. Chu, J.T. Butcher, Rapid 3D printing of anatomically accurate and mechanically heterogeneous aortic valve hydrogel scaffolds, Biofabrication 4 (2012), 035005, https://doi.org/10.1088/1758-5082/4/3/035005.
- [64] M. Bydon, A.B. Dietz, S. Goncalves, F.M. Moinuddin, M.A. Alvi, A. Goyal, Y. Yolcu, C.L. Hunt, K.L. Garlanger, A.S. del Fabro, R.K. Reeves, A. Terzic, A.J. Windebank, W. Qu, CELLTOP clinical trial: first report from a phase 1 trial of autologous adipose tissue–derived mesenchymal stem cells in the treatment of paralysis due to traumatic spinal cord injury, Mayo Clin. Proc. 95 (2020) 406–414, https://doi.org/10.1016/j.mayocp.2019.10.008.
- [65] A. Thomas, I. Orellano, T. Lam, B. Noichl, M.-A. Geiger, A.-K. Amler, A.-E. Kreuder, C. Palmer, G. Duda, R. Lauster, L. Kloke, Vascular bioprinting with enzymatically degradable bioinks via multi-material projection-based stereolithography, Acta Biomater. 117 (2020) 121–132, https://doi.org/10.1016/j.actbio.2020.09.033.